PROCEEDINGS, 43rd Workshop on Geothermal Reservoir Engineering
Stanford University, Stanford, California, February 12-14, 2018
SGP-TR-213

Advanced Polymer-Modified Cements for Subsurface Applications

Carlos A. Fernandez,* Kenton A. Rod, Nicholas Huerta, and Phillip K. Koech

902 Battelle Blvd, Richland, WA, 99352

Carlos.Fernandez@pnnl.gov

Keywords: Geothermal, wellbore, cement, polymer, self-healing

ABSTRACT

Wellbore failure at the cement lining is one of the most common drivers of reservoir intervention during geothermal energy and unconventional oil/gas production. The main sources for cement fracturing are chemical, mechanical, and thermal stresses. As a result, expensive and time-intensive production shutdowns and repairs are required. Intervention costs average $1.5million per wellbore without taking into consideration the economic losses as a result of production stoppage, which can be several million dollars depending on the time frame of plant in non-production mode. To address these problems, we developed a thermally stable polymer-cement composite with self-healing properties while maintaining the required rheological (during pumping) and mechanical properties of typical wellbore cement. In this work we report on the composition and mineralogy, the mechanical properties and self-healing ability of these novel cement composites as compared to standard wellbore cement. The self-healing capability of the composite materials was demonstrated by the consistent permeability reduction of mechanically-induced fractures in the 0.3-0.5mm aperture range. These polymer-cement composite materials could represent a definite solution to wellbore failure, production stoppage and reservoir intervention during geothermal energy production.

1. INTRODUCTION

Long-term mechanical stability of a cement sheath exposed to stresses in a geothermal wellbore environment is critical to maintaining zonal isolation for the life of the well. Wellbore stresses of sufficient magnitude to cause failure of a cement sheath may result from changes in casing pressure, temperature, formation pressure, or near- wellbore tectonic stresses.[1] The ability of a cement sheath to remain intact when exposed to changing wellbore stresses is highly dependent upon mechanical properties including ductility and tensile strength of the cement and the surrounding rock.[2]

A great deal of research is dedicated to the development of advanced cements with desired mechanical properties, thermal stability including resistance to thermal shock, and resilience to different chemical environments found in geothermal wellbores, including high mineral acid, high brine concentrations, and highly carbonated environments. Cement formulations with both inorganic and organic additives have been developed to be deployed for geothermal wellbore operations. Among the cements reported comprise phosphate-bonded cement,[3, 4] organic and semi- inorganic cement materials,[5] foam cements,[6] and other cement formulations designed to improve upon OPC.[7, 8] Despite significant advancement in development of cementitious materials for geothermal applications and self-healing cements in general,[9, 10] self-healing cements with improved adhesion at both the casing and formation interfaces under geothermal conditions have yet to be developed.[4, 11, 12] Cement with self-healing properties is a path toward long-term geothermal wellbore integrity that diminishes the need for expensive interventions.

Pacific Northwest National Laboratory (PNNL) has recently developed a novel polymer-cement composite for geothermal wellbore applications by simple addition of disulfide containing epoxies to well cement. This polymer-cement combination leads to cement slurries with rheological properties comparable to those of standard well cement while the compressive strength of is lower than that of standard cements, they are still high (>3000psi) and well above the requirements for geothermal well cementing.[13]

Here we report the mechanical properties of this polymer-cement composites including Young Modulus, fracture toughness, self-healing ability and resistance to different geothermal environments including concentrated mineral acid, highly concentrated CO_2 in brines, and thermal shock cycles as evaluated by monitoring compressive strength before and after material's weathering.

2. MATERIALS AND METHODS

2.1 Cement Synthesis

The control and polymer-cement composites were synthesized as previously reported (Table S1).[17] Class H cement was supplied by LaFarge from the Joppa Plant. Silica flour (200 mesh) was obtained from U.S. Silica. Thioplast EPS 25 (EPS 25) (640 g/1 equivalent epoxide) was supplied by Akzo Nobel, and 4-dimethylaminopyridine (DMAP), poly(ethylene glycol) diglycidyl ether (PEO) (250 g/1 equivalent epoxide) and pentaerythritol tetrakis (3-mercaptopropionate) (4SH) were purchased from Sigma-Aldrich. All materials were used as received. Cement samples were synthesized by mixing the class H cement powder and silica flour in a poly(propylene) beaker, then adding deionized (DI) H_2O and mixing to give a cement slurry. The slurry was transferred to plastic molds approximately 2.54 cm in diameter by 10.16 cm in length. Molds were placed in a small container which was then inserted inside a larger vessel containing water and covered in Al foil. This setup was placed in an oven and the samples were cured at 85 ºC for 24 hours. Polymer-cement composites were synthesized by adding the monomers mixture to the cement slurry and thoroughly mixing to give polymer-cement slurries (Table

1). Similarly, the polymer-cement mixtures were cured in a high humidity environment at 85 ºC for 24 hours. Both cement and polymer-cement composite samples were then removed from the molds and cured in a 2L autoclave vessel with 30 mL of H_2O at 200 ºC for an additional 5 days. The polymer concentration in the composites was 10 wt% for all tests.

Table 1. Composition of cement and polymer-cement composite

Component	Cement	10% Polymer- cement
Cement (g)	157.5	157.5
Silica flour (g)	67.5	67.5
Water (g)	85.5	112.5
Water:cement	0.54	0.71
Total polymer (g)	0	22.5
EPS 25 (g)	0	8.40
EPS 25 (mmol)	0	6.60
PEO (g)	0	8.40
PEO (mmol)	0	16.8
4SH (g)	0	5.70
4SH (mmol)	0	11.7

2.2 Tomography

Tomography of cement samples were conducted at both Environmental and Molecular Sciences Laboratory (EMSL; Richland WA) and at the SRX Beamline (Brookhaven NY). At EMSL a Nikon XTH 320/225 X-ray CT instrument was used to obtain 3D volume data at up to 20-50 µm resolution on sections of cement cores (depending on specimen size), which can then be viewed as sliceable images on the computer and analyzed for structural and density changes. We collected X-ray computed tomography (XCT) images of each piece at high resolution, so that each exposed and unexposed sample could be compared. The 3D data on the cement was then processed in ImageJ (ImageJ: Image Processing and Analysis in Java. Available from: http://imagej.nih.gov/ij/ (2017)) to enhance contrast, and the density or structural changes were emphasized with the WEKA segmentation tool in ImageJ/Fiji. The different colors of the segmentation classes' show were the treatment effects the samples.

Full-field tomography experiments were conducted at the SRX Beamline (5-ID, NSLS-II). A monochromatic X-ray beam with 20 kV energy was selected using Si (111) double-crystal monochromator. A total of 1441 image projects were collected on the sample in each tomographic measurement, over 180° angular range (0.125° step size), using pco.edge 5.5 CMOS camera. The images were corrected by dark field images, normalized by white field images, and then aligned using a tomographic data collected on a calibration pin to remove the systematic lateral and vertical displacements.

Tomographic reconstruction was conducted with filtered back projection algorithm using TomoPy, a python based software[14] to reconstruct each set of projections into a 3-dimensional (3D) tomographic dataset. Each reconstructed 3D XCT image dataset was cropped to a volume of 665 × 715 × 880 pixels (Each voxel size is 2.03 × 2.03 × µm3) for analysis. A median filter-based smoothing algorithm was then applied to the reconstructed 3D images in freeware Image J.[15] Segmentation was conducted with a thresholding value determined from the histogram of reconstructed images. Artifacts in the segmented 3D images were removed in software Avizo (v.9.0, FEI). The artifact removed 3D images were imported to ImageJ for measuring porosity by voxel counting and to dragonfly software (v.2.0, ORS) for analyzing the pore/particle size distribution. The 3D volume visualization was conducted in Avizo.

2.3 Evaluation of Mechanical Properties

2.3.1 Compressive Strength

Cement monoliths with an average length of 8.2 cm (±0.5) and diameter of 2.5 cm (±0.03) were tested for compressive strength using standard methods (ASTM C39/C39M-15a). Before conducting tests the monolith ends were cut, using a rock saw, perpendicular to the length to provide a flat surface minimizing point loading during tests. Tests were performed using a MTS model 312.31 servohydraulic frame with a 55 kip actuator and load cell. The loading rate was 0.24 MPa/s and cardboard shims were placed between the plate and sample on both ends to absorb potential point loading from sample defects that could increase the risk of test failure. Tests were conducted in triplicate for each condition. Replicated samples were compared for significant differences using a multi comparison ANOVA, one tail Tukey test. After testing, selected crushed samples were healed at 200 °C for five days and then retested for compressive strength. Standard laboratory Parafilm was wrapped around the samples to prevent them from crumbling during the initial compression test and healing process.

2.3.2 Fracture Toughness

Fracture toughness was tested on cement samples with an average width of 2.5 cm (±0.05), thickness of 2.5 cm (±0.04), and a span of 7.6 cm. The samples were tested using standard methods.[1] Before conducting the tests all edges of the tests were trimmed of surface imperfections with a rock saw, yielding cuboids with smooth surfaces. A 0.5 mm wide notch was cut at the midpoint of cement samples to a depth of 1.2 cm (±0.04). Tests were performed using a MTS model 312.31 servohydraulic frame at a loading rate of 0.025 cm minute^{-1}.

2.3.3 Young Modulus

To calculate Young's Modulus we measure stress and strain data during mechanical testing of the specimens. Tests are performed using an MTS 312.21 servohydraulic universal test frame controlled by Instron Bluehill 2 software. Samples were spatter painted before testing, creating dark contrasting speckles on light colored surface. Stress-strain data was collected using video capture of compression tests with the prepared samples, measuring movements of speckles relative to each other. Load and displacement data is collected during testing and used to calculate stress and strain in the sample throughout the test. The stress-strain curve generated is used to determine the Young's modulus. The elastic modulus of the sample is the ratio of stress to strain in the sample which is calculated by determining the slope of the curve in the elastic region of the test.

2.4 Permeability Measurements

Cement monoliths with an average length of 4.1 cm and diameter of 2.5 cm (±0.03) were tested for fracture permeability using deionized (DI) water. Cured samples were cut to length with a rock saw, and the sides bound with heavy-duty moisture-seal heat-shrink tubing after removing glue from the tubing. These monoliths were then placed upright in a hydraulic press with thick metal plates placed on either end covering only half of each end and with the top plate offset from the bottom plate. Force (444–667 N) was applied to the monolith with the offset plates until a shear fracture occurred along the longitudinal axis. Fractured samples were fitted with PTFE tubing end caps using a combination of heat-shrink tubing and ring clamps (Figure 2). Permeability was tested using the saturated constant head method[16] where constant head was maintained by maintaining the reservoir (sealed vessel) at a constant air pressure (102 cm water at 4 °C) and discharge was measured at atmospheric pressure. Reynolds equation (Equation 1)[17] for flow through fractured media with Darcy's law (Equation 2), with cross sectional area being the aperture times width (Wb) of the fracture, was arranged for calculation of permeability (Equation 3):

$$\boldsymbol{Q = -\frac{Wb^3}{12v}\left(\frac{P_0 - P_i}{l}\right)} \qquad \textit{Equation 1}$$

$$\boldsymbol{Q = -\frac{k_i Wb}{v}\left(\frac{P_0 - P_i}{l}\right)} \qquad \textit{Equation 2}$$

$$\boldsymbol{k_i = \frac{b^2}{12}} \qquad \textit{Equation 3}$$

Where: Q = discharge (cm^3 s^{-1}); W = effective fracture width (cm); b = effective aperture of fracture (cm); v = kinematic viscosity of water (cm^2 s^{-1}); $P_0 - P_i$ = Pressure change across fracture length (cm water at 4 °C); l = length of sample (cm); k_i = permeability (cm^2). For the calculations the effective fracture width (W) was estimated to be the diameter of the monolith as the shear fracture was applied across the center-point at each end of the monolith.

2.5 Infrared and X-ray Spectroscopy

Transmission Fourier Transform Infrared spectroscopy (FTIR) was performed on a Nicolet iS10 spectrometer by mixing ground cement (1–2%) with KBr followed by preparation of a pellet. Spectra were baseline corrected and analyzed using OMNIC software. For the crosslinked polymer, attenuated total reflectance (ATR) mode was used on a freshly cut polymer surface.

Powder X-ray diffraction (XRD) analysis was obtained from cement and polymer-cement composite samples placed on 0.8 mm capillaries. A custom-built environmental stage inside a Bruker-AXS D8 Discover XRD unit equipped with a rotating Cu anode (1.54 Å), Göbel mirror, 0.5 mm collimator, and 0.5 mm pin hole (Madison, WI) was used. Powder samples were aligned using a video laser alignment system. Patterns were collected with a GADDS® area detector positioned at 21°2θ and 40°2θ with a measured distance from the sample of 15 cm. Collection of individual XRD tracings required 300 s with power settings of 50 kV and 24 mA. Images were processed with Bruker-AXS GADDS software before importing into JADE® XRD software to obtain peak positions and intensities.

3. RESULTS AND DISCUSSIONS

3.1 Mineralogy and Chemistry

Portland cement H or G subjected to high temperatures, as in geothermal wellbores, develop different mineral phases of calcium silicates and calcium aluminum silicates form. The presence and stability of these phases depend on temperature, the original composition of the cement mixture, the water-to-cement ratio, and the SiO_2-to-CaO ratio. The cement composition used in this work is a class H cement mixed with silica flour in a cement-to-silica flour ratio of 70:30. The SiO_2:CaO molar ratio was 1.05, and the water-to-cement ratio (w:c) for base cement was 0.54. The curing process consisted in 24h at8 5°C, followed by curing at 200°C for 5 days at 99+ % relative humidity. The expected dominant mineral phases based on these conditions are xonolite [$Ca_6Si_6O_{17}$- $(OH)_2$] and SiO_2 with some percentage of gyrolite [$NaCa_{16}$- $Si_{23}AlO_6(OH)_8 \cdot 14H_2O$].[18] Portland cement used in typical wellbore completions has high compressive strength, but relatively weak tension and adhesion.

As predicted, XRD spectra of base cement and 10wt% polymer-cement composite both cured at 200 °C (Figure 1) showed as dominant phases xonolite[19] and quartz (due to the additional SiO_2 added). No difference in XRD pattern was observed between cement and polymer-cement composite demonstrating that the presence of 10wt% of tetrathiol-crosslinked thermoset epoxide EPS25 does not affect the mineralogical composition of cement H.

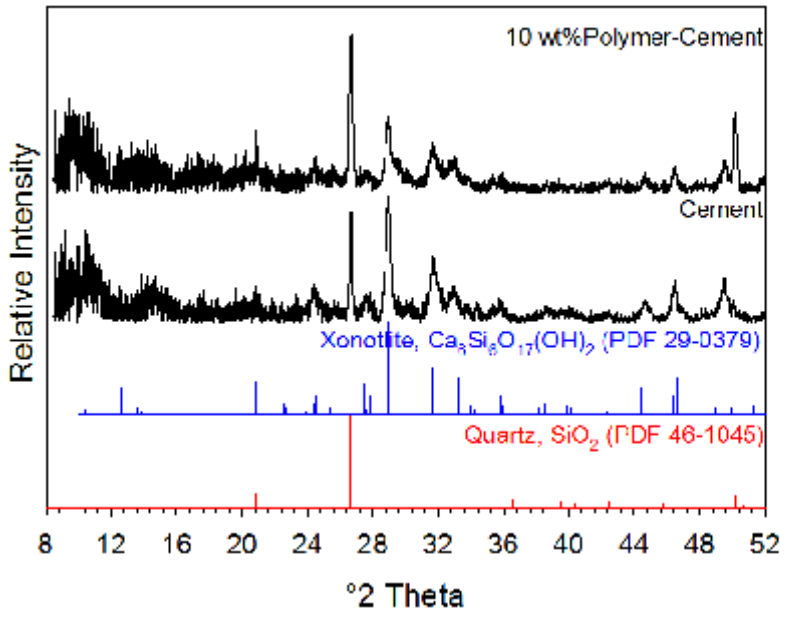

Figure 1. XRD spectra of polymer-cement composite (top) and base cement (bottom). XRD peaks for Xonolite and quartz are shown in blue and red, respectively.

To determine if the polymer was indeed present in the cement matrix we examined the FTIR spectrum of powdered cement and polymer-cement samples (Figure 2). Little difference was seen in the spectra of the cement and the 10 wt % polymer-cement samples, though the strong absorption bands due to water in the cement phases45,46 made it difficult to observe the regions most likely to show polymer absorption bands (O−H stretching near 3300 cm^{-1}, H−C−H symmetric and antisymmetric stretching near 2900 cm^{-1}, C=O stretching near 1725 cm^{-1}). Preparation of a more polymer concentrated sample (25 wt % polymer, w:c of 0.86, 28-day cure at 22 °C) gave an FTIR spectrum where the H−C−H symmetric and antisymmetric stretching modes of the polymer are clearly visible near 2925 and 2875 cm^{-1}. The FTIR spectrum of the same polymer-cement system cured for 1 day at 85 °C and 5 days at 200 °C shows less prominent, but still visible, H−C−H symmetric and antisymmetric stretching bands.

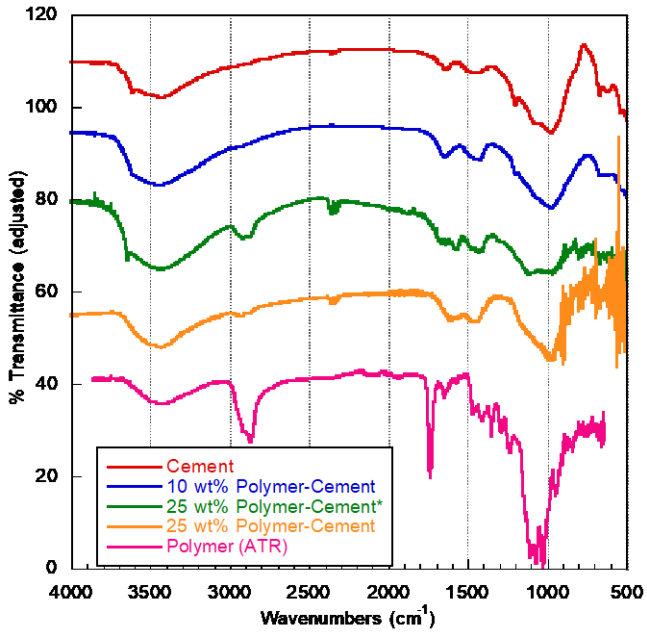

Figure 2. FTIR spectra of cement samples, cement has a w:c of 0.54 and was cured for 1 day at 85 °C then 5 days at 200 °C, 10 wt% Polymer-Cement has a w:c of 0.71 and was cured for 1 day at 85 °C then 5 days at 200 °C, 25 wt% Polymer-Cement* has a w:c of 0.86 and was cured for 28 days at 22 °C, 25 wt% Polymer-Cement has a w:c of 0.86 and was cured for 1 day at 85 °C then 5 days at 200 °C.

3.2 Mechanical Properties

The mechanical strength of wellbore cement determines its ability to resist stress at depth and thus minimize fracturing, reducing the probability of wellbore intervention. The strengths of the cement and the polymer-cement samples were assessed with standard compressive strength[22], fracture toughness and Young Modulus test methods to measure resistance to compressive and tensile forces present in the wellbore environment as well as to determine the material's ductility and how the polymer presence affects it.[23, 24] For the compressive strength evaluation, a series of replicate tests were conducted on samples. The polymer-cement composites require a minimum w:c of 0.71 to have a homogenous slurry with similar flowability to base cement. The base cement samples were prepared with the typical w:c ratio of 0.54 and, for comparative purposes, w:c ratio of 0.71. Base cement and 10wt% polymer-cement were cured for 28 days at 85 °C and +99% relative humidity and the compressive strength determined. For base cement with w:c ratio of 0.54 and 0.71 the compressive strength was 4801 ± 670 psi and 2727 ± 330 psi, respectively. The polymer-cement samples with w:c of 0.71 showed an average compressive strength of 1784 ± 160 psi. The results (Table 2) show that there is a decrease in compressive strength when 10wt% of polymer is added to cement independently of the larger w:c ratio used to prepare the slurry. Curing the base cement and polymer-cement samples at more representative geothermal temperatures, 200 °C, boost the compressive strength significantly for both base cement 43%, 6875 ± 260 psi as expected. The higher curing temperature however has higher impact in the compressive strength of the polymer-cement composites which nearly doubles in value at 200 °C, 3350 ± 90 psi as compared to 1784 ± 160 psi when cured at 85 °C for 28 days.

Wellbore cement is subject to not only compressive forces but also tensile forces at the interfaces resulting from faults in the subsurface. To compare base cement to 10wt% polymer-cement composites, duplicates of fracture toughness tests were conducted on specimens cured at 85 °C for 28 days (Table 2) with the standard dimensions described in the Materials and Methods section. With no polymer, the critical stress intensity factor was 0.011 $MN \cdot m^{-3/2}$ for 0.54 w:c and 0.015 $MN \cdot m^{-3/2}$ for 0.71 w:c, respectively. Similar to compressive strength, the addition of polymer to the cement mixture reduced the critical stress intensity factor, with measured values of 0.007 $MN \cdot m^{-3/2}$ for 10wt % polymer-cement samples with 0.71 w:c. The preferred minimum criteria for the critical stress intensity factor is 0.006 $MN \cdot m^{-3/2}$, suggesting again that 10 wt % polymer is probably the maximum polymer concentration for acceptable mechanical properties in the polymer-cement composite formulations.

Young's Modulus analysis, a measure of tensile elasticity of materials, was determined for control cement and 10 wt% polymer-cement composites in triplicate (Table 2). For control cement, an average Young's modulus of (1.7 ± 0.6) x 10^6 psi was obtained, while for the polymer-cement composites the average value was (1.0 ± 0.1) x 10^6 psi, 40% lower than base cement. As importantly, the strain map as a function of stress applied for control cement and polymer-cement composite samples was significantly different. The strain map for the control cement samples consistently showed a heterogeneous distribution of strain as a function of stress applied throughout the entire course of the test (Figure 3, left). On the other hand, the strain maps of the 10 wt% polymer-cement composites show a homogeneous distribution of strain in the entire the sample (Figure 3, right), that also uniformly increases with stress applied, until the very end where mechanical failure occurs. This suggests that the polymer-cement composites may be relatively more elastic/ductile than pure cement samples which allow them to better respond against mechanical stress.

Table 2. Mechanical properties of base cement and 10wt% polymer-cement composites

Sample	Curing conditions	Compressive strength (psi)	Fracture toughness (MN·m−3/2)	Young's Modulus (psi)
Base cement	85°C/28d, w:c=0.54	4801 ± 670	0.011	N/A
Base cement	85°C/28d, w:c=0.71	2727 ± 330 psi	0.015	N/A
10wt% polymer-cement	85°C/28d, w:c=0.71	1784 ± 160	0.007	N/A
Base cement	85°C/1d + 200°C/5d, w:c=0.54	6875 ± 260	N/A	(1.7 ± 0.6) x 10^6
10wt% polymer-cement	85°C/1d + 200°C/5d, w:c=0.71	3350 ± 90	N/A	(1.0 ± 0.1) x 10^6

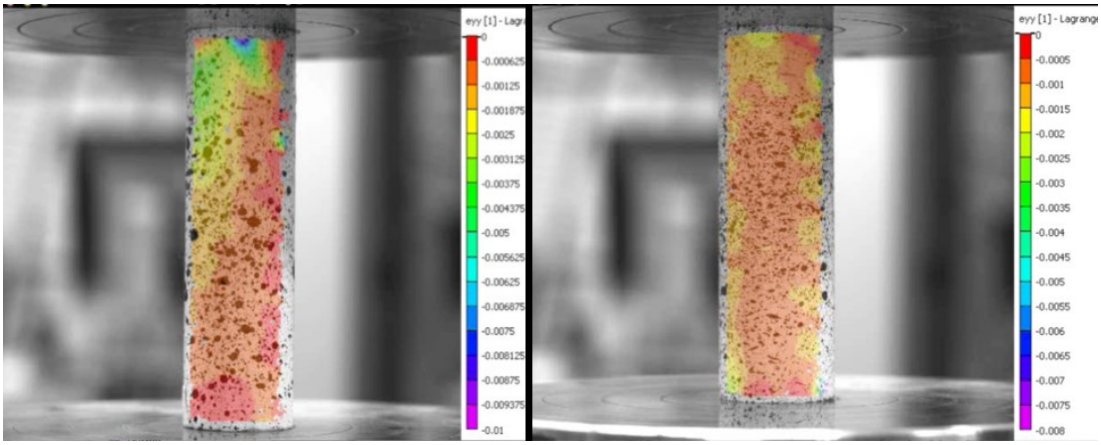

Figure 3. Strain distribution map for a given, identical, applied pressure to base cement (left) and 10wt% polymer-cement composite (right). Note the heterogeneous distribution of strain throughout the sample in base cement as compared to the more homogeneous strain distribution for the cement composite. This was observed through the entire course of the test.

3.3 Permeability Results

Cement fractures due to tensile and shear stress (tensile and shear failure) are among the major failure modes of wellbore cement. Thus, to learn about the ability of the polymer-cement composites to self-heal shear fractures permeability measurements were performed after generating a tensile fracture and then again after healing the fractured samples at 200 °C for 5 days. The fracture extends across the full diameter of the cylinders and across the entire cylinder's length. The tests were performed by triplicate in both base cement and polymer-cements. The values are shown in Table 3. Base cement shows a small decrease or an increase in permeability while the 10 wt % polymer-cement samples consistently show significant decrease in permeability values by −87%, −60%, and −62% after healing (Figure 4, left). When comparing the percent change of permeability between the control samples and the polymer-cement samples, the change is significant (ANOVA, Tukey, 0.05). The effective aperture before healing for the samples was in the range of 0.3 – 0.5 mm. These results are remarkable considering that typical fracture apertures in geothermal wellbore cement are in the 5−20 μm range. The polymer-cement composite materials show significant self-healing capability and structural integrity even when the fractures created are over an order of magnitude larger than typical fractures encountered in wellbore cement (Figure 4, right).

Table 3. Permeability values before and after cement samples healing event. Positive change signifies a reduction in permeability.

Sample	Curing conditions	Permeability before healing (cm2)	Permeability
Base cement #1	85°C/1d + 200°C/5d, w:c=0.54	1.7×10^{-4}	1.5
Base cement #2	85°C/1d + 200°C/5d, w:c=0.54	2.7×10^{-4}	2.2
Base cement #3	85°C/1d + 200°C/5d, w:c=0.54	5.0×10^{-4}	7.0
10wt% polymer-cement #1	85°C/1d + 200°C/5d, w:c=0.71	9.1×10^{-5}	1.2
10wt% polymer-cement #2	85°C/1d + 200°C/5d, w:c=0.71	2.7×10^{-4}	1.1
10wt% polymer-cement #3	85°C/1d + 200°C/5d, w:c=0.71	2.1×10^{-4}	7.9

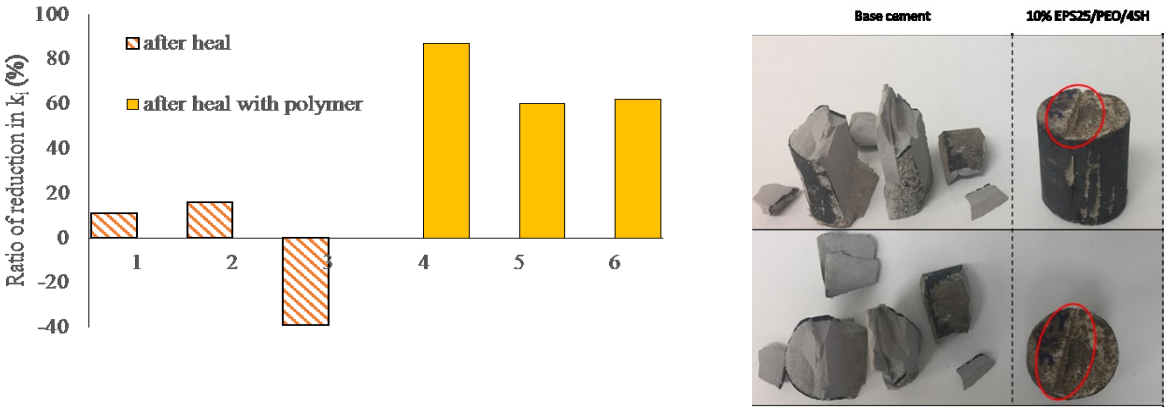

Figure 4. Left. Permeability change after a 5-day/200 °C healing events for base cement (orange pattern), and 10wt% polymer-cement composites (solid yellow). Right. Representative samples of base cement and 10wt% polymer-cement composites after shrink wrap holding samples together was removed. Notice the healed fracture and superior structural integrity of the composite material.

3.4 Tomography Analysis

XMT analysis was performed as described in the Materials and Methods section on both base cement and 10wt% polymer-cement composites. The main observation was the larger number of voids found in the cement composite. It is important to mention that the w:c ratio for the preparation of polymer-cements was larger (w:c=0.71) than the ratios used for base cement (w:c=0.54). Then, the larger concentration of voids in the cement composite could be due to the excess (unreacted) water evaporating during curing leaving voids behind. Most of the voids are filled, partially or completely, by polymer and potentially explained by the high flowability of the polymer precursors and polymeric products at the elevated curing temperatures rapidly filling the void spaces left behind by the excess (evaporating) water during the curing process (Figure 5). Although not a direct measurement of porosity, the specific surface area of the cement could be influenced by the presence of porosity and micro-porosity. The surface area results show that there is little to no difference between the control cement (15.9 m^2 g^{-1}), and the 10 wt% polymer-cement composite (16.1 m^2 g^{-1}). This could be due to a combination of factors including the cement having low permeability for gas, the pores (voids) are not interconnected, and (in the case of polymer-cement) the existing pores are filled with polymer. Each of these factors could contribute to the similar specific surface area measurements. Based on XMT data it is observed that the polymers do fill these voids and that the voids seem to have no connectivity (Figure 5). Since most of the voids formed during the curing process in the polymer-cement composite are filled with polymer the total volume of air void is lower (0.22 % of the total volume) than the total volume of air void for control cement (0.44 % air void). Assuming a polymer density of 1 g/mL the polymer content estimated from the 3D XCT images (Figure 5) for 10 wt% polymer-cement composites was 11.4 wt%.

The polymer-cement composites also showed larger concentration of high density unhydrated cement grains throughout the material (Figure 5). The polymer filled pores along with the unhydrated grains possibly explains the lower compressive strength in the polymer-cement composite samples. As it will be described in the next section the polymer-cement composite shows self-healing behavior. The self-healing capability of these polymer-cement composites could be associated to the presence of a "reservoir" of latent polymer and uncured (unhydrated) cement ready to flow (polymer) and react in the event of material's damage. The presence of homogeneously distributed polymer throughout the cement matrix seems critical for the self-healing capability of the composite material and its higher ductility.

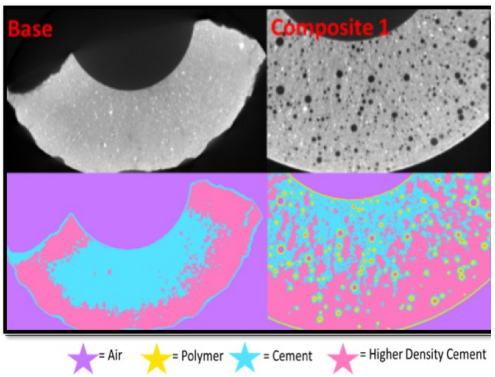

Figure 5. X-Ray microtomographs with density contrast analysis to identify polymer, air voids, and higher density cement. Left corresponds to base cement showing a small concentration of voids as compared to the polymer-cement composite with a larger concentration of voids, the majority of them filled with polymer (in yellow).

4. SUMMARY

In summary, we have presented a novel class of polymer-cement composites with mechanical properties that make them suitable for their application as wellbore cements. We have demonstrated that the mineralogy is similar to base cement in absence of the polymer and that the polymer is homogeneously distributed across the cement matrix. A larger concentration of void spaces is observed in the composite materials with most of these (not interconnected) voids filled with polymer. The presence of polymer throughout the cement matrix seems to bring ductility to the composite material as evidenced by a 40% decrease in the Young's Modulus respect to base cement. The self-healing capability of these polymer-cements was demonstrated by the consistent reduction in permeability on tensile fractures with apertures as large as 0.3−0.5 mm. Future work will focus on evaluating the capability of these composites to resist typical geothermal environments, including highly concentrated brines, mineral acid, CO_2, as well as thermal shock.

REFERENCES

1. Nelson, E. B.; Guillot, D.; Eds., *Well Cementing*. 2nd ed.; Schlumberger: Sugar Land, TX, 2006.
2. Shortall, R.; Davidsdottir, B.; Axelsson, G., Geothermal energy for sustainable development: A review of sustainability impacts and assessment frameworks. *Renew. Sust. Energ. Rev.* **2015,** *44*, 391-406.
3. Rockett, T. J.; McEwen, E. E.; Clappin, J. P.; Feng, S. S.; Ouellette, A. J.; Thakore, N. C.; Yuh, S. J. Phosphate-Bonded Glass Cements for Geothermal Wells; Report BNL 51153; Brookhaven National Laboratory/U.S. Department of Energy: Washington, DC, 1979.
4. Sugama, T. Advanced Cements for Geothermal Wells; Report BNL- 77901-2007-IR; Brookhaven National Laboratory/U.S. Department of Energy: Washington, DC, 2006.
5. Zeldin, A. N.; Kukacka, L. E.; Carciello, N. Polymer-Cement Geothermal-Well-Completion Materials; Brookhaven National Laboratory/U.S. Department of Energy: Washington, DC, 1980.
6. Bour, D. L.; Hernandez, R. CO2 Resistance, Improved Mechanical Durability, and Successful Placement in a Problematic Lost-Circulation Interval Achieved: Reverse Circulation of Foamed Calcium Aluminate Cement in a Geothermal Well. GRC Trans. 2003, 27, 163−167.
7. Roy, D. M.; White, E. L.; Langton, C. A.; Grutzeck, M. W. New High Temperature Cementing Materials for Geothermal Wells: Stability and Properties; Report BNL 51249; Brookhaven National Laboratory/ U.S. Department of Energy: Washington, DC, 1980.
8. Finger, J.; Blankenship, D. Handbook of Best Practices for Geothermal Drilling; Report SAND2010-6048; Sandia National Laboratories/U.S. Department of Energy: Washington, DC, 2010.
9. Van Tittelboom, K.; De Belie, N. Self-Healing in Cementitious Materials: a Review. Materials 2013, 6, 2182−2217.
10. Wu, M.; Johannesson, B.; Geiker, M. A Review: Self-Healing in Cementitious Materials and Engineered Cementitious Composite as a Self-Healing Material. Constr. Build. Mater. 2012, 28, 571−583.
11. Zeldin, A. N.; Kukacka, L. E.; Carciello, N. *Polymer-cement-geothermal-well-completion materials*; Brookhaven National Laboratory/U.S. Department of Energy: Washington, DC, 1980.
12. Rockett, T. J.; McEwen, E. E.; Clappin, J. P.; Feng, S. S.; Ouellette, A. J.; Thakore, N. C.; Yuh, S. J. *Phosphate-bonded glass cements for geothermal wells, BNL 51153*; Brookhaven National Laboratory/U.S. Department of Energy: Washington, DC, 1979.
13. Childers, M. I.; Nguyen, M. T.; Rod, K. A.; Koech, P. K.; Um, W.; Chun, J.; Glezakou, V. A.; Linn, D.; Roosendaal, T. J.; Wietsma, T. W.; Huerta, N. J.; Kutchko, B. G.; Fernandez, C. A., Polymer-Cement Composites with Self-Healing Ability for Geothermal and Fossil Energy Applications. *Chem. Mat.* **2017,** *29*, (11), 4708-4718.
14. Snoeck, D.; Dewanckele, J.; Cnudde, V.; De Belie, N., X-ray computed microtomography to study autogenous healing of cementitious materials promoted by superabsorbent polymers. *Cement & Concrete Composites* **2016,** *65*, 83-93.
15. Todorovic, J.; Raphaug, M.; Lindeberg, E.; Vralstad, T.; Buddensiek, M. L., Remediation of Leakage through Annular Cement Using a Polymer Resin: a Laboratory Study. In *8th Trondheim Conference on Co2 Capture, Transport and Storage*, Aarlien, R.; Rokke, N. A.; Svendsen, H. F., Eds. Elsevier Science Bv: Amsterdam, 2016; Vol. 86, pp 442-449.
16. Klute, A.; Dirksen, C., Hydraulic Conductivity and Diffusivity: Laboratory Methods. In *Methods of Soil Analysis, Part 1 - Physical and Mineralogical Methods*, Klute, A., Ed. American Society of Agronomy, Inc, Soil Science Society of America, Inc,: Madison, WI, 1986; pp 687-734.
17. Nicholl, M. J.; Rajaram, H.; Glass, R. J.; Detwiler, R., Saturated Flow in a Single Fracture: Evaluation of the Reynolds Equation in Measured Aperture Fields. *Water Resour. Res.* **1999,** *35* (11), 3361-3373.
18. Nelson, E. B.; Barlet-Gouéd́ard,V. Thermal Cements. In Well Cementing, 2nd ed.; Nelson, E. B., Guillot, D., Eds.; Schlumberger: Sugar Land, TX, 2006.
19. Pernites, R. B.; Santra, A. K. Portland Cement Solutions for Ultra-High Temperature Wellbore Applications. Cem. Concr. Compos. 2016, 72, 89−103.

20. Ghosh, S. N.; Handoo, S. K. Infrared and Raman Spectral Studies in Cement and Concrete (Review). Cem. Concr. Res. 1980, 10, 771−782.

21. Hughes, T. L.; Methven, C. M.; Jones, T. G. J.; Pelham, S. E.; Fletcher, P.; Hall, C. Determining Cement Composition by Fourier Transform Infrared Spectroscopy. Adv. Cem. Based Mater. 1995, 2, 91−104.

22. Standard Test Method for Compressive Strength of Cylindrical Concrete Specimens; ASTM C39/C39M-15a; ASTM Internation: West Conshohocken, PA, 2015.

23. Rockett, T. J.; McEwen, E. E.; Clappin, J. P.; Feng, S. S.; Ouellette, A. J.; Thakore, N. C.; Yuh, S. J. Phosphate-Bonded Glass Cements for Geothermal Wells; Report BNL 51153; Brookhaven National Laboratory/U.S. Department of Energy: Washington, DC, 1979.

24. Petersson, P. E. Fracture Energy of Concrete - Method of Determination. Cem. Concr. Res. 1980, 10, 79−89.